

Investigation of the Stable Atmospheric Boundary Layer at Halley Antarctica

Javier Sanz Rodrigo · Philip S. Anderson

Received: 23 November 2012 / Accepted: 16 May 2013 / Published online: 18 June 2013
© Springer Science+Business Media Dordrecht 2013

Abstract Boundary-layer measurements from the Brunt Ice Shelf, Antarctica are analyzed to determine flux–profile relationships. Dimensionless quantities are derived in the standard approach from estimates of wind shear, potential temperature gradient, Richardson number, eddy diffusivities for momentum and heat, Prandtl number, mixing length and turbulent kinetic energy. Nieuwstadt local scaling theory for the stable atmospheric boundary-layer appears to work well departing only slightly from expressions found in mid-latitudes. An $E-l_m$ single-column model of the stable boundary layer is implemented based on local scaling arguments. Simulations based on the first GEWEX Atmospheric Boundary-Layer Study case study are validated against ensemble-averaged profiles for various stability classes. A stability-dependent function of the dimensionless turbulent kinetic energy allows a better fit to the ensemble profiles.

Keywords Antarctica · Flux–profile relationships · Local scaling · Mixing length · Stable boundary layer · Richardson number

1 Introduction

The surface layer in Antarctica is largely influenced by the presence of persistent radiative cooling, especially during wintertime (King and Turner 1997). This cooling generates

J. S. Rodrigo
von Karman Institute, Sint-Genesius-Rode, Belgium

P. S. Anderson
British Antarctic Survey, Cambridge, UK

P. S. Anderson
Scottish Association for Marine Science, Oban, UK

J. S. Rodrigo (✉)
National Renewable Energy Centre of Spain (CENER), Sarriguren, Spain
e-mail: jsrodrigo@cener.com

significant temperature gradients in the atmosphere near the surface and thence leads to a stably-stratified atmospheric boundary layer. In the absence of wind-driven mixing, this SBL is characterized by low turbulence and a shallow boundary-layer depth. In mid-latitudes, stable conditions develop during nighttime over land when the surface is radiatively cooled and, over the sea, a stable boundary layer (SBL) may develop when warm air is advected over colder water.

The stable boundary layer has been the subject of numerous studies due to inherent difficulties when applying traditional scaling rules. In effect, the neutral and unstable regimes are more dominated by turbulent mixing and their structure is better understood using similarity theories. Some of the features that characterize the SBL are described by Mahrt (1999) e.g. intermittency, the appearance of gravity waves and meandering, the layering of turbulence and the absence of a well-defined boundary-layer depth. Although there are numerous studies devoted to the SBL, a unified theory for the very stable regime does not as yet exist. This is partly due to the difficulty of measuring intermittent turbulence and partly due to the co-existence of different phenomena with different turbulent origins (Mahrt 1999).

Intermittency is a characteristic of very stable regimes, when brief episodes of turbulence appear sporadically within otherwise relatively weak background turbulence. Similarity theories are used to reduce the degrees of freedom of the flow's behaviour by organizing the flow variables into dimensionless groups that are related to underlying scaling relationships. Similarity relationships are usually found in steady-state or equilibrium conditions. In the atmospheric boundary-layer (ABL) context, they are used to relate turbulent fluxes with bulk variables, such as wind and temperature gradients, so that equilibrium profiles can be derived for the mean variables and the turbulence statistics as a function of height. Boundary-layer models can then be constructed relying on the observed scaling functions. Popular mixing-length models allow an efficient characterization of the SBL by means of eddy-viscosity turbulent closures.

Nieuwstadt (1984) analyzed stable-condition turbulence measurements from a meteorological mast in Cabau, The Netherlands. He showed that the dimensionless equations for turbulence variances and covariances lead to a local scaling hypothesis, whereby dimensionless combinations of variables measured at the same height can be expressed as a function of a single parameter $\zeta = z/L$, where z is the height above the ground and L is the local Obukhov length:

$$L = -\frac{u_*^3}{\kappa \frac{g}{\Theta_0} w\theta}, \quad (1)$$

defined in terms of the local friction velocity (u_*), the von Karman constant ($\kappa = 0.41$), the gravitational acceleration ($g = 9.81 \text{ m s}^{-2}$), a reference potential temperature (Θ_0) and the local kinematic heat flux ($w\theta$), with w and θ being fluctuations from their respective means. As a result, local scaling theory is a generalization of Monin–Obukhov similarity theory (MOST) beyond the surface layer. Therefore, with local scaling it is possible to describe the structure of the whole of the SBL.

Sorbjan (2010) and Sorbjan and Grachev (2010), proposed a gradient-based similarity approach whose scales are defined in terms of the vertical velocity variance and the Brunt–Väisälä frequency. We here look for differences between the Antarctic SBL and that found in mid-latitudes by comparing flux–profile expressions derived from the Halley 2003 dataset with functional forms from the literature based on local scaling similarity. While differences are noted, we show that mid-latitude formulations can still be used with confidence for the simulation of SBL structure.

2 The Halley 2003 Experiment

Polar regions are natural laboratories for the study of the SBL (King and Turner 1997). The long fetches over the ice shelf with uniform and flat terrain allow easier characterization of the lower boundary conditions. The winter darkness allows persistent radiative cooling for days or weeks at a time, without any diurnal variation, leading to strong potential temperature gradients. A wide range of stability regimes can be studied at a single location.

The measurements analyzed in this work were made in the Clean Air Sector of the British Antarctic Survey's Halley Research Station (75.6°S, -26.7°E) between March and November 2003; hence the data are dominated by low sun angles or winter darkness. In 2003, Halley was situated towards the seaward edge of the Brunt Ice Shelf. The ice shelf extends some 40 km to the south-east of Halley before rising to the continental plateau at 3,000 m altitude. A homogeneous upwind fetch of 100 km, with no appreciable terrain rise coupled with an aerodynamically smooth surface makes the site ideal for micrometeorological studies. The prevailing wind direction at Halley is from the east, especially at high wind speeds. The absolute humidity of the air is low in general due to the low temperatures. However freezing fog can encourage the accumulation of rime ice on the instruments (King and Anderson 1988).

King (1990) studied the validity of surface-layer similarity over the ice shelf in Halley during the first STable Antarctic Boundary-Layer Experiment (STABLE) in the austral winter of 1986 (King and Anderson 1988). The analysis of the neutral wind profile revealed a dynamic roughness length of 10^{-4} m, the same value found by König (1985) on a similar ice shelf. Such a small value is related to the fine structure of the snow surface rather than to the sastrugi. King and Anderson (1994) analyzed again the roughness length and found a value of 6×10^{-5} m, again similar to the previous finding based on the STABLE data.

The dataset analyzed in this study is the same as that used by Anderson (2009). A 32-m high lattice mast was equipped with turbulence and profile instruments mounted on 2-m long booms. The instruments include:

- Three heated sonic anemometer/thermometers situated at heights of 4, 16 and 32 m of the USA-1 (Metek GmbH) type.
- Five platinum resistance thermometers Vaisala HMP45 with R.M. Young aspirated radiation shields at 1, 2, 4, 8, 16 and 32 m.
- Five R.M. Young propeller/vane anemometers also situated at 1, 2, 4, 8, 16 and 32 m.
- A snow accumulation sensor, to adjust the sensor heights throughout the measurement campaign.

The sonic anemometers were sampled at 20 Hz while the wind vector and temperature were recorded as 10-min averages. Turbulence variances and covariances were calculated over 1-min average periods after correcting for the instrument tilt, and removing spikes and linear trends within each 1-min interval. The choice of a short interval aims at reducing the bias of the turbulent fluxes in the range of very high stability, where measurements are less reliable and similarity functions are challenged. Klipp and Mahrt (2004) used a 100-s window as the gap scale that separates high-frequency from sub-mesoscale turbulence under strong stability conditions in the Cooperative Atmosphere-Surface Exchange Study (CASES-99) experiment in Kansas. Under weakly stable conditions Klipp and Mahrt (2004) state that a longer interval is necessary but the resulting net error is lower than the random flux error. Since Halley is characterized by much larger stabilities than Kansas, we believe that choosing a shorter time scale is appropriate. Vickers and Mahrt (2003) showed that the gap scale is rather independent of the measurement height above the ground in stable conditions.

Throughout the year, a net snow accumulation of around 1.2 m is found over the Brunt Ice Shelf. This accumulation reduces the effective height of the sensors and, therefore, it has been considered in the analysis of profile data.

3 Flux–Profile Analysis

The 1-min turbulence and 10-min profile data are averaged to 1-hr intervals to obtain a synchronized dataset. Similar averaging windows are used by Klipp and Mahrt (2004) for flux calculations in the SBL. One-hour intervals are required in order to reduce random flux errors and avoid excessive scatter in the flux–profile analysis. The data were quality controlled prior to the flux–profile analysis in order to remove spurious or low-quality records. The analysis of dimensionless gradients in stable conditions requires very significant filtering on the dataset in order to avoid excessive scatter Anderson (2009). Table 1 shows the filtering criteria adopted in this study together with the number of hourly samples remaining after each filtering step.

To avoid shadowing effects from the mast, records were only accepted if the wind direction was within a $90 \pm 60^\circ$ (true) sector. Profiles with excessive wind direction shear between the top and bottom of the mast were also removed as in Yagüe and Redondo (1995). This will remove some outliers from the analysis even though this may include an extreme wind veering effect (Ekman-type spiral) observed in the Antarctic (Dabberdt 1970; Lettau and Dabberdt 1970) and in the Arctic (Grachev et al. 2005).

Frost effects are identified following the same procedure of Anderson (2009), that is, based on the relative velocity difference between sonic, U_{sonic} , and propeller, U_{prop} , anemometers at the same level,

$$|\Delta U| = \left| \frac{U_{\text{sonic}} - U_{\text{prop}}}{U_{\text{sonic}} + U_{\text{prop}}} \right|, \tag{2}$$

when the relative difference is larger than 10 %, the hourly profile is discarded.

Much of the scatter can be eliminated by removing data with very low turbulence and near-zero fluxes and gradients. Small flux data are characterized by larger measurement errors and

Table 1 List of quality-control filters and % of remaining data samples

Filter	Criteria	Levels	Samples	%
Instrument malfunctions		4, 16 and 32 m	7,344	83.8
Wind-direction sector with no mast distortion	$90 \pm 60^\circ$	16 m	4,490	51.3
Excessive wind-direction change	$<20^\circ$	Between 4 and 32 m	3,769	43.0
Remove registers affected by frost effects	$ \Delta U < 0.1$	4, 16 and 32 m	1,870	21.3
Remove near-zero fluxes	$-w\theta > 0.002 \text{ m K s}^{-1}$	4, 16 and 32 m	811	9.3
Study stable atmospheric conditions	$L > 0$	4 m	678	7.7
Remove low shear profiles ($X = [U; \theta]$)	$dX/dz > 0.001 \text{ [s}^{-1}; \text{K m}^{-1}]$	4, 16 and 32 m	252	2.9
Remove extreme shear profiles ($X = [U; \theta]$)	$dX/dz < 0.4 \text{ [s}^{-1}; \text{K m}^{-1}]$	4, 16 and 32 m	233	2.7

may be more dominated by mesoscale trends (Klipp and Mahrt 2004). Hence, minimum thresholds in the kinematic heat flux (0.002 m K s^{-1}), velocity (0.001 s^{-1}) and temperature (0.001 K m^{-1}) gradients are set. The selection of the thresholds is based on the impact in the scatter of the flux–gradient plots. Higher thresholds eliminate more scatter but also reduce the number of samples. Even though the near-zero-flux filter will also remove samples in the near-neutral regime, it is more convenient for a clearer picture of the stable regime. Finally a few profiles showing too low and too large velocity shear or temperature gradient have also been removed, where the local shear is obtained by fitting log-linear functions to the measurements as is described in the next section. As a result, only 2.7% of the original data, corresponding to 233 profiles, are retained for the analysis of flux–profile relationships.

3.1 Dimensionless Velocity and Temperature Gradients

Even though several instrument levels are available for the calculation of the velocity and temperature gradients by finite differences, it is more accurate to derive the local gradients after the profile-fitting method of Nieuwstadt (1984). In effect, the velocity and temperature profiles take the log-linear form:

$$X = P_1 z + P_2 \ln z + P_3, \quad (3)$$

where X can be either U or θ and P_i are regression coefficients obtained by least-squares fitting to hourly profiles with six levels. Local gradients are easily obtained for any height:

$$\frac{\partial X}{\partial z} = P_1 + \frac{P_2}{z}. \quad (4)$$

The velocity and temperature gradients can be made non-dimensional making use of the kinematic turbulent fluxes measured by the sonic anemometers. The friction velocity is calculated from the momentum fluxes:

$$u_* = (\overline{uw^2} + \overline{vw^2})^{1/4}. \quad (5)$$

According to Sorbjan (1986), based on Monin–Obukhov similarity theory, the dimensionless velocity, $\phi_m(\zeta)$, and temperature, $\phi_h(\zeta)$, gradient given by

$$\phi_m(\zeta) = \left(\frac{\kappa z}{u_*} \right) \frac{\partial U}{\partial z} \quad (6)$$

and

$$\phi_h(\zeta) = \left(\frac{\kappa z}{\theta_*} \right) \frac{\partial \Theta}{\partial z}, \quad (7)$$

are functions of the stability parameter ζ , where $\Theta_* = -\overline{w\theta}/u_*$ is a temperature scale. This dependency is found at Halley when the three sonic levels are plotted together (Fig. 1 for the velocity gradient and Fig. 2 for the potential temperature gradient). In these figures, light grey points indicate registers not passing the last four filters of the quality control of Table 1. On top of the individual samples, bin averages have been included for easier interpretation of the measured trends, with error bars indicating one standard deviation of the ensemble within each bin.

Several forms of stability functions are also presented in Figs. 1 and 2,

$$\phi_x(\zeta) = a_x + b_x \zeta, \quad (8)$$

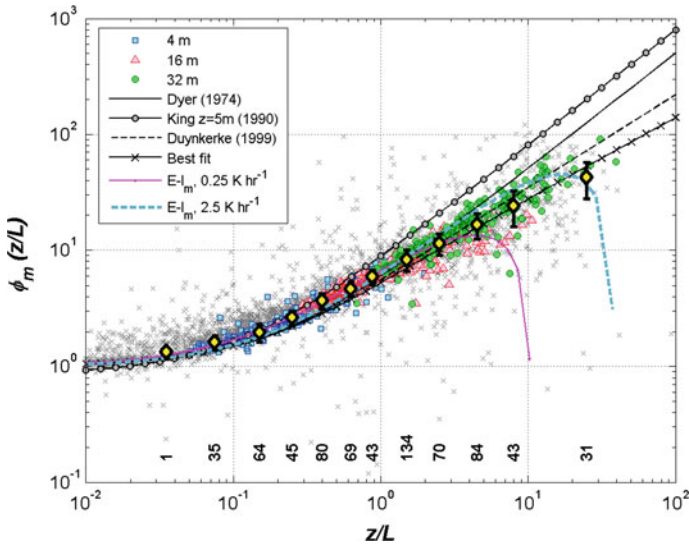


Fig. 1 Dimensionless gradient of wind velocity based on local scaling from measurements at [4,16,32] m, functional forms and $E-I_m$ model simulations of Sect. 4. Grey crosses represent filtered-out data. Bin averages of filtered-in data are given in yellow diamonds and include error bars for one standard deviation

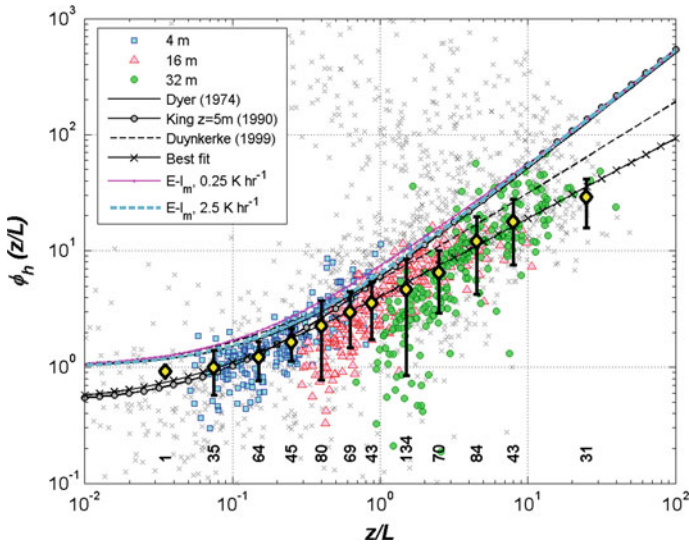


Fig. 2 Dimensionless gradient of temperature based on local scaling from measurements at [4,16,32] m, functional forms and $E-I_m$ model simulations. Grey crosses and yellow error bars are as per Fig. 1

with $a_m = a_h = 1$; $b_m = b_h = 5$,

$$\phi_x(\zeta) = a_x + b_x \zeta, \tag{9}$$

with $a_m = 0.85$; $a_h = 0.49$; $b_m = 8$; $b_h = 5.4$,

$$\phi_x(\zeta) = 1 + b_x \left(1 + \frac{b_x}{a_x} \zeta \right)^{a_x - 1} \quad (10)$$

with $a_m = a_h = 0.8$; $b_m = 5$; $b_h = 7.5$, where x is m or h and the functions were obtained respectively from experiments in Kansas, U.S.A. (Dyer 1974), Halley (Antarctica) (King 1990) and Cabauw, Netherlands (Duynerke 1999). A review of the numerical coefficients b_m and b_h can be found in Hogstrom (1988), Sorbjan (1989), and Garratt (1992). Other interpolation functions for ϕ_x obtained from CASES-99 and SHEBA (Surface Heat Budget of the Arctic Ocean) experiments can be found in Cheng (2005) and Grachev et al. (2007a) respectively. The SHEBA experiment took place in 1997–1998 over Arctic ice while the CASES-99 experiment was conducted in 1999 over flat terrain in Kansas.

It is instructive to note the large scatter before and after application of the quality control. In the near-neutral limit, all the samples were filtered out by the minimum heat-flux threshold. Nevertheless, the discarded samples in this near-neutral limit show ϕ_m values between 0.9 and 2, with 1 being a likely mean value. The scatter in the near-neutral range can be attributed to the sensitivity of roughness length with stability, as indicated by Zilitinkevich et al. (2008), who found a range of 50 times higher z_0 in neutral conditions than in very stable conditions ($\zeta = 5$).

In the case of ϕ_h the neutral limit is less clear. These values and the general trend of the data agree reasonably well with classical mid-latitude functional forms from Dyer and Duynerke and contradict some of the conclusions from King (1990), who found a neutral limit of 0.85 preventing the wind profile from taking the well-known logarithmic form. In fact, Duynerke's formulation is superior to Dyer's in the high stability range ($\zeta > 1$), predicting lower values of the dimensionless gradients than Dyer's functions.

The bin averages in ϕ_h indicate that classical functions from mid-latitudes might over-predict the temperature gradient. An alternative functional form based on Duynerke's formulation (10) is obtained by manually adjusting the coefficients to obtain the best fit to the results of this dataset: $a_m = a_h = 0.7$, $b_m = 5$, $b_h = 7.5$ ("best fit" in Figs. 1 and 2). Nevertheless, considering the large scatter of the data and the large number of functional forms already available in the literature it is suggested to keep the classical forms for the sake of universality in both middle and high latitudes. Hence, Dyer's functional forms will be adopted for SBL modelling in this study. This was also concluded by Handorf et al. (1999) after a flux–profile experiment in the Neumayer Antarctic station. Dyer's forms are also supported by large-eddy simulation (LES) modelling and theoretical analysis (Zilitinkevich et al. 2010).

Yagüe et al. (2001) reanalyzed the STABLE dataset during the winter period March–August 1986; at the 5-m level, they showed good agreement with classical stability functions as well. Both Yagüe et al. (2001) and King (1990) found some indication of z -less stratification: at large stabilities dimensionless quantities tend to level off as a limiting behaviour of local scaling (Nieuwstadt 1984). According to Nieuwstadt, when $\zeta \gg 1$, turbulence scales are so small, due to the strong attenuation of vertical motion by stable stratification, that the presence of the ground is no longer felt and the dependency of flux–gradient parameters with z disappears. Nieuwstadt found this limit in the Cabauw data for $\zeta > 1$. In terms of the dimensional velocity and temperature gradients, z -less stratification regime is found when these become independent on z . If ϕ_x are linear functions of z/L the gradients tend to a constant value at large z/L (Wyngaard and Coté 1972). Thus the levelling-off of ϕ_x is evidence of the breakdown of z -less stratification. Based on the 2003 dataset we note evidence of levelling-off at $\zeta > 10$ but it is difficult to confirm due to the large scatter and the few samples of the dataset in this regime. In effect, the very high stability regime is affected by the

rejection of small flux measurements during the quality control of the data. If these data are not filtered out, however, spurious bin averaging is likely to occur (Grachev et al. 2012), wherein near-neutral data can be mistaken for very stable data, both sharing very low heat fluxes.

Sorbjan (2010) and Sorbjan and Grachev (2010) analyzed flux–profile relationships based on data collected during the SHEBA and CASES-99 experiments. Even though the same procedure for flux calculations was adopted in both experiments, the datasets differ in the level of mesoscale “contamination” since this is very site dependent. In spite of these differences, the datasets showed good agreement in the flux–profile relationships. Similar differences are seen in the Halley 2003 data also due to mesoscale effects.

The analysis of dimensionless gradients versus the stability parameter is contaminated by the presence of self-correlation, which happens when one or more variables appears in the functions represented in both axes of the scatter plot. This is the case for the friction velocity, which forms the definition of both L and ϕ_x . Self-correlation can artificially create trends in the data that are not necessarily present in reality. Unfortunately the level of self-correlation is not straightforward to evaluate. According to Baas et al. (2006), ϕ_m is more affected by self-correlation because the scatter is roughly aligned with the physical curve, giving the impression of a better correlation. The contrary occurs with ϕ_h whose scatter is roughly perpendicular to the physical curve. This partly explains the large scatter of ϕ_h compared to ϕ_m . While self-correlation occurs in both ϕ_m and ϕ_h , the effect is only significant in the case of ϕ_m . Although the scatter is severely affected by self-correlation in ϕ_m , the slope of the curve is not (Baas et al. 2006). The dimensionless temperature gradient is not sensitive to self-correlation and shows the true scatter. As the Obukhov length depends on u_* , small uncertainties in the calculation of this variable can be significant.

Klipp and Mahrt (2004) analyzed the impact of self-correlation and intermittency in flux–profile relationships. A conditional analysis was constructed in order to filter out samples with high intermittency that violated the assumption of stationarity necessary for turbulent scaling laws. By removing intermittent episodes, the scatter in the plot was generally reduced and many of the outlying samples in the high stability range moved towards the steady-state functional forms.

The use of a gradient-based similarity approach as proposed by Sorbjan (2010), which is based on gradient Richardson number instead of z/L , significantly reduces the self-correlation problem (Sorbjan and Grachev 2010).

Non-stationary data will mostly affect the range of high stabilities, where the samples are characterized by very small turbulence scales. This is typical of the upper part of the boundary layer, where the flow tends to be intermittent and heterogeneous and functional steady-state forms are not applicable (Zilitinkevich and Esau 2007).

3.2 Richardson Number

The gradient Richardson number (Ri) and the flux Richardson number (Ri_f) are defined as follows

$$Ri(\zeta) = \frac{\frac{g}{\Theta_0} \frac{\partial \Theta}{\partial z}}{\left(\frac{\partial U}{\partial z}\right)^2} = \zeta \frac{\phi_h(\zeta)}{\phi_m^2(\zeta)}, \quad (11)$$

$$Ri_f(\zeta) = \frac{-\frac{g}{\Theta_0} \overline{w\theta}}{u_*^2 \frac{\partial U}{\partial z}} = \frac{\zeta}{\phi_m(\zeta)}. \quad (12)$$

The experimental results of Nieuwstadt indicated a critical Richardson number in the limit of large stabilities; this was identified with a z -less stratification regime. Zilitinkevich and Esau (2007) argued that the concept of a critical Ri contradicted experimental evidence since much larger values could be found (Zilitinkevich et al. 2010).

The concept of a critical Ri was recently revisited by Grachev et al. (2013) to determine the limits of applicability of local similarity theory. By spectral analysis of the velocity and temperature fluctuations they showed that, when the gradient and flux Richardson numbers exceed a critical value of about 0.2–0.25, the Kolmogorov inertial subrange dies out, indicating an upper limit for the applicability of the local Monin–Obukhov (and z -less) theory. Using $Ri_c > 0.2$ –0.25 and $Ri_{fc} > 0.2$ –0.25, the latter as primary threshold, it was possible to filter out data points where Monin–Obukhov similarity fails. This resulted in non-dimensional velocity and temperature gradients closely following the classical linear forms of Dyer. If this filter was not applied, the stability functions showed a slower increase with increasing ζ than the ones predicted by Dyer, as is also observed in the current dataset (Figs. 1, 2). Kouznetsov and Zilitinkevich (2010) concluded that any form of ϕ_m that increases below $5z/L$ under strong stability implies a supercritical flux Richardson number and is thus inconsistent with the assumption of homogeneous stationary turbulence, i.e. with local similarity theory. This typically happens in the upper part of the SBL and in the free atmosphere, hence the critical Richardson number is sometimes used to determine the height of the SBL (Handorf et al. 1999; Zilitinkevich and Baklanov 2002).

Zilitinkevich et al. (2013) propose a hierarchy of turbulence closure models for the SBL that assumes that turbulence is maintained by the velocity shear at any gradient Richardson number, and distinguishes between two regimes: “strong turbulence” when $Ri \ll 1$ typical of boundary-layer flows and “weak turbulence” at $Ri > 1$ typical of the free atmosphere or deep ocean.

Figure 3 shows the dependency of Ri_f with the stability parameter. As noticed by Yagüe et al. (2001), King’s relation is well suited for moderate stabilities but underpredicts Ri_f for large ζ . Dyer’s parametrization predicts an asymptotic limit to $Ri_{fc} = 0.2$ which, in this case,

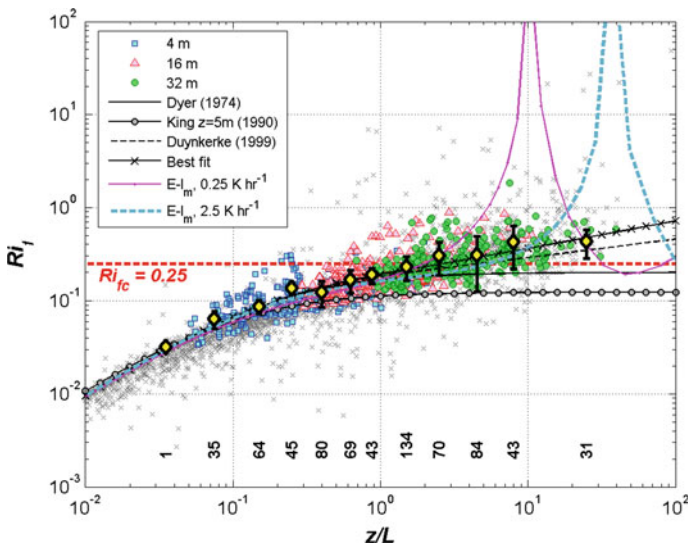


Fig. 3 Flux Richardson number based on local scaling from measurements at [4,16,32] m, functional forms and $E-I_m$ model simulations. Grey crosses and yellow error bars are as per Fig. 1

underpredicts Ri_f at high stabilities. Duynkerke’s parametrization presents a better fit with the data, showing an increase of Ri_f at high stabilities beyond $Ri_{fc} = 0.25$.

Sorbjan and Grachev (2010) found that Ri_c was reached in the SHEBA data at $\zeta \approx 4$. Above this Ri increased to 0.5 for $\zeta \approx 100$, as with Duynkerke’s function, but above this the scatter is significant although $Ri > 1$ can be found. It is also worth mentioning that the gradient-based similarity approach results in an expression of $Ri(\zeta)$ that is free of self-correlation.

Comparison of curve and data points in Fig. 4 of Sorbjan and Grachev (2010) shows a departure for $\zeta > 1$ that is attributed to self-correlation. In the case of Ri_f , part of the differences observed in Fig. 3 between data and classical functional forms could be also attributed to self-correlation.

Sorbjan and Grachev (2010) identified four stable regimes based on $Ri(\zeta)$: near-neutral ($0 < \zeta < 0.02$ or $0 < Ri < 0.02$), weakly stable ($0.02 < \zeta < 0.6$ or $0.02 < Ri < 0.12$), very stable ($0.6 < \zeta < 50$ or $0.12 < Ri < 0.7$) and extremely stable ($\zeta > 50$ or $Ri > 0.7$). Marked differences in the trends were found between the near-neutral (linear function) and the very stable (exponential function) regimes. The extremely stable regime is not found in the Halley dataset. It is also noted that a large number of samples show Ri_f above the critical value, though many of these large values shall correspond to samples above the SBL, where the flow is neither stationary nor homogeneous. Note that the range of stabilities in the SBL is typically $\zeta < 10$ and that some profiles reach Ri_{fc} at the 16- and 32-m levels, indicating a very low boundary-layer depth.

A critical flux Richardson $Ri_{fc} = 0.2$ was found by Zilitinkevich et al. (2010), from theoretical analysis and LES data, as the inverse of the slope of the dimensionless wind shear in the very stable limit, i.e. $b_m = 1/Ri_{fc}$ in (8). Hence Dyer’s expression is supported by empirical, numerical and theoretical arguments, a good reason to take it as a universal function in boundary-layer parametrizations.

3.3 Turbulent Diffusivities and Prandtl Number

Turbulent diffusivities can be obtained using eddy-viscosity theory that relates the kinematic turbulent fluxes for momentum and heat to the velocity and temperature gradients:

$$K_m = -\frac{\overline{wu}}{\partial U/\partial z}, \tag{13}$$

$$K_h = -\frac{\overline{w\theta}}{\partial \Theta/\partial z}. \tag{14}$$

The ratio of K_h and K_m is the inverse Prandtl number:

$$Pr^{-1} = \frac{K_h}{K_m} = \frac{Ri_f}{Ri}. \tag{15}$$

Figure 4 shows the stability dependence of the turbulent diffusivities for momentum and heat, made non-dimensional by dividing by the local u_*L ; the inverse Pr is also shown. As for the dimensionless gradients (Figs. 1, 2), the eddy viscosity shows less scatter than the eddy conductivity due to self-correlation. This effect was also observed for the SHEBA data (e.g., Grachev et al. 2005, 2007a). The dimensionless eddy viscosity grows with stability. Nieuwstadt found an asymptotic value of 0.07, which is significantly exceeded here in the high stability range.

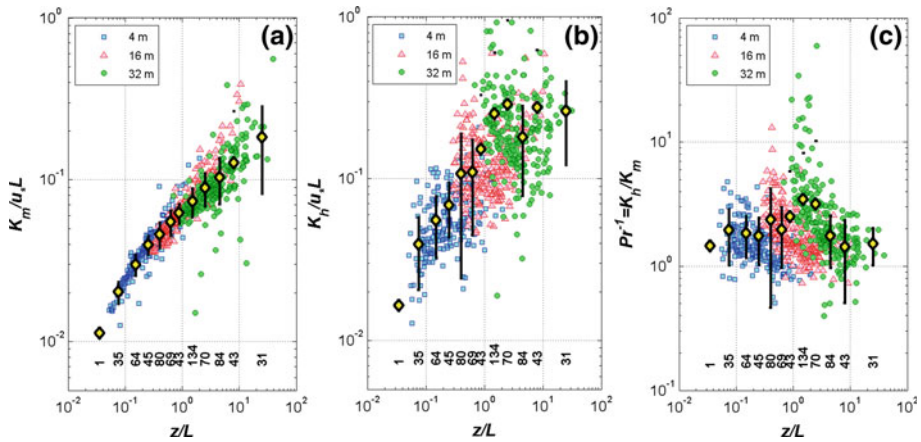


Fig. 4 Stability dependence of the dimensionless eddy viscosity for momentum (a) and heat (b), and the inverse *Pr* number (c). Bin averages of filtered-in data include error bars for one standard deviation

The bin averages of the eddy conductivity may suggest an asymptotic behaviour at high stabilities, but it is difficult to confirm due to the large scatter. In any case, the asymptotic limit would be around 0.3, much higher than the value of 0.07 found by Nieuwstadt.

The *Pr* number is rather independent of stability with an average value of 0.5 in the observed stability range. It is uncertain how self-correlation affects these results. Anderson (2009) studied the dependency of the inverse *Pr* with *Ri* using a technique free of self-correlation and constant *Pr* values were also found when *Ri* < 0.1. Sorbjan and Grachev (2010) also found fairly constant values of *Pr* around 0.83 for the SHEBA data. From this experiment, Grachev et al. (2007b) found that *Pr* decreases with increasing stability using the bulk Richardson number to avoid self-correlation. The CASES-99 dataset showed more scatter and lower mean values of 0.3–0.4 for *Ri* < 0.2 (Sorbjan and Grachev 2010), closer to the values found at Halley.

3.4 Mixing Length

The mixing length is an important scaling factor in the description of the vertical structure of the ABL, related to the integral length scale of the microscale turbulence spectrum. The mixing length, l_m , is defined as (Mahrt and Vickers 2003):

$$l_m = \frac{u_*}{\partial U / \partial z} = \frac{\kappa z}{\phi_m}, \tag{16}$$

which can be extracted from the flux–profile analysis. First-order turbulence closure schemes use this parameter as a length scale for the eddy viscosity as will be shown below. Blackadar (1962) proposed an analytical expression for the mixing length in the neutral ABL where l_m was proportional to the height near the surface and approached an asymptotic value, λ , at greater heights, which can be parametrized based on the geostrophic wind G or with the friction velocity u_* ,

$$l_m = \frac{\kappa z}{1 + \frac{\kappa z}{\lambda}}, \tag{17a}$$

$$\lambda = 2.7 \times 10^{-4} \frac{G}{|f_c|}, \tag{17b}$$

$$\lambda = 6.3 \times 10^{-3} \frac{u_*}{|f_c|}, \tag{17c}$$

where f_c is the Coriolis parameter defined as $f_c = 2\Omega\sin\gamma$ ($\Omega = 7.27 \times 10^{-5} \text{ s}^{-1}$ is the earth’s angular velocity and γ is the latitude). Djolov (1973) and Delage (1974) extended Blackadar’s formulation to account for stability

$$l_m = \frac{\kappa z}{\phi_m(\zeta) + \frac{\kappa z}{\lambda}}, \tag{18}$$

where Djolov used surface-layer scaling and Delage used local Obukhov length scaling in the definition of ϕ_m . Sun (2011) analyzed the validity of Monin–Obukhov theory and Blackadar’s formulation to describe the vertical structure of the mixing length during CASES-99 experiment. Mahrt and Vickers (2003), also based on CASES-99 data, evaluated a number of mixing-length formulations. They propose a so-called hybrid similarity theory since it is a generalization of (18) and approaches MOST near the surface and z -less prediction at higher ζ levels. The hybrid theory includes a dependence on the boundary-layer depth. Boundary-layer height has also been suggested as an additional parameter by Gryning et al. (2007).

Figure 5 shows the dimensionless mixing length, l_m , as a function of the stability parameter z/L . l_m is normalized by the surface-layer mixing length κz ; as a result Fig. 5 represents the inverse of ϕ_m , i.e. the inverse of Fig. 1. In the neutral boundary layer $l_m \approx 40 \text{ m}$, which is an order of magnitude larger than found in the very stable conditions observed at Halley. These small turbulence scales (1 m) constitute the main drawback when simulating the SBL with LES models due to the high grid resolution required to resolve the majority of the significant eddies (Beare et al. 2006).

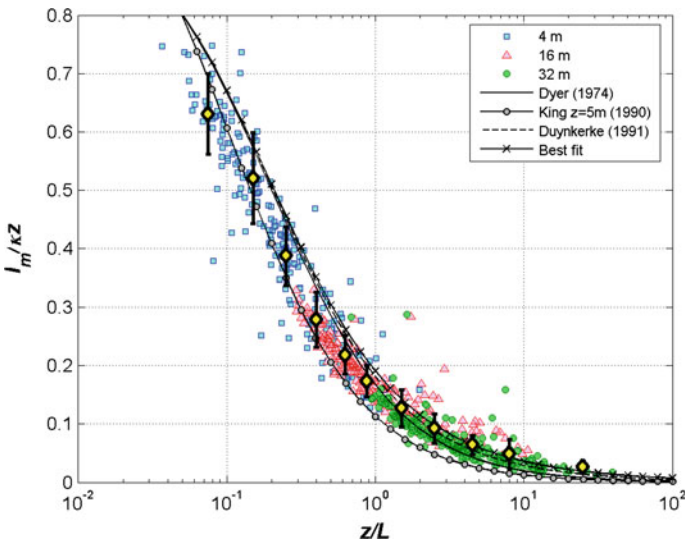


Fig. 5 Stability dependence of the mixing length. Data points at [4,16,32] m levels are obtained by using (16) and mixing-length parametrizations are based on (18)

The agreement of the functional forms is reasonably good and present rather low scatter, as per ϕ_m , due to the presence of self-correlation. This shows that the mixing length is a robust scaling parameter that does not depend so much on the selected functional form.

3.5 Turbulent Kinetic Energy

Turbulence in first-order closure models is considered via the solution of the turbulent kinetic energy (E) transport equation (also called 1.5-order closure). This bulk quantity accounts for the energy content of the turbulent eddies and it is defined as

$$E = \frac{1}{2} (\overline{u^2} + \overline{v^2} + \overline{w^2}). \tag{19}$$

The eddy viscosity can then be written,

$$K_m = \alpha^{1/2} l_m E^{1/2}, \tag{20}$$

where α is a constant. In neutral, stationary and local equilibrium conditions, when production and dissipation of turbulence is balanced, an expression for α can be found from the E transport equation,

$$\alpha = \frac{u_*^2}{E} \tag{21}$$

whose standard value from laboratory and numerical experiments in neutral conditions is $\alpha_0 = 0.3$ (Zilitinkevich et al. 2010). The inverse of α is plotted in Fig. 6 as a dimensionless form for E . At neutral to moderate stabilities the non-dimensional E is roughly constant, equal to $1/0.22 = 4.5$, i.e. higher than the standard value of $1/0.3 = 3.3$. Above $\zeta > 0.5$ the non-dimensional E grows until it reaches the boundary-layer top around $\zeta = 10$. Above this value an asymptotic value is assumed.

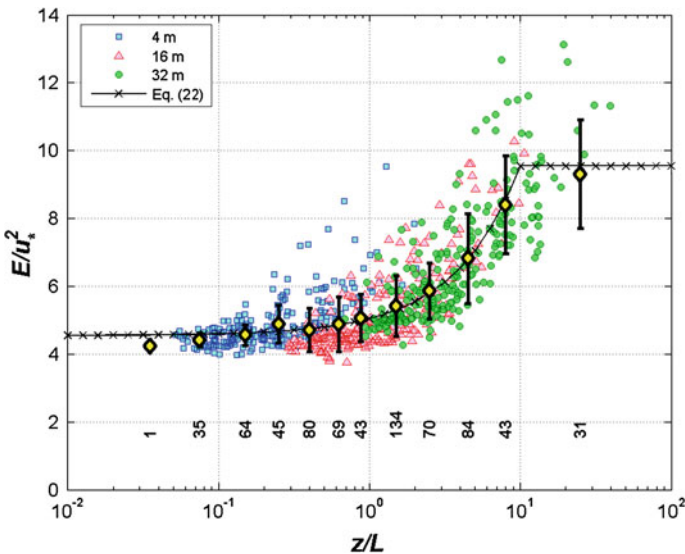


Fig. 6 Stability dependence of turbulent kinetic energy

The values of dimensionless E obtained at Halley agree with values reported by Zilitinkevich et al. (2010), equal to 3–5 in the near-neutral range and increasing to 10–15 in the very stable limit ($Ri > 10$). This dependency of E on stability was also found by Freedman and Jacobson (2003), who derived an analytical expression for α which depended on the local Ri by imposing consistency with local scaling theory. A simpler empirical parametrization can be obtained from the experimental data at Halley:

$$\frac{E}{u_*^2}(\zeta) = \frac{1}{\alpha} = \begin{cases} \frac{1}{\alpha_0} + b_E \zeta & \zeta \leq 10 \\ \frac{1}{\alpha_0} + b_E 10 & \zeta > 10 \end{cases} \tag{22}$$

where $\alpha_0 = 0.22$ is the value in the neutral limit and $b_E = 0.5$.

4 Single-Column Model of the Stable ABL

Flux–profile analysis will now be used to parametrize a single-column model of the SBL. In horizontally homogeneous (unlimited upwind fetch) conditions, the Reynolds-averaged momentum equations are

$$\frac{\partial U}{\partial t} = -f_c(V - V_g) + \frac{\partial}{\partial z} \left(K_m \frac{\partial U}{\partial z} \right), \tag{23a}$$

$$\frac{\partial V}{\partial t} = f_c(U - U_g) + \frac{\partial}{\partial z} \left(K_m \frac{\partial V}{\partial z} \right), \tag{23b}$$

where the geostrophic equilibrium allows the introduction of the mean geostrophic wind components (U_g, V_g) in place of the horizontal pressure gradients

$$U_g = -\frac{1}{f_c \rho} \frac{\partial p}{\partial y}, \tag{24a}$$

$$V_g = \frac{1}{f_c \rho} \frac{\partial p}{\partial x}, \tag{24b}$$

where ρ is the air density. The viscous terms are defined in terms of the eddy viscosity. Similarly, the energy equation after Reynolds-averaging and neglecting radiative effects is reduced to

$$\frac{\partial \Theta}{\partial t} = \frac{\partial}{\partial z} \left(K_h \frac{\partial \Theta}{\partial z} \right), \tag{25}$$

where dry air is assumed (that is, no phase-change energy transfer is added) and K_h is related to K_m via the Prandtl number (15). Hence, closure of the SBL model is attained by defining the eddy viscosity. A review of first-order turbulent closure schemes can be found in Holt and Raman (1988). One-equation closure introduces a prognostic equation for the turbulent kinetic energy

$$\frac{\partial E}{\partial t} = \frac{\partial}{\partial z} \left(K_e \frac{\partial E}{\partial z} \right) + G_E - \varepsilon, \tag{26}$$

where G_E is the production of E and ε is the turbulent dissipation rate. The diffusion coefficient K_e is assumed equal to K_m . Turbulent kinetic energy is produced by wind shear and buoyancy

$$G_E = -\overline{uw} \frac{\partial U}{\partial z} - \overline{vw} \frac{\partial V}{\partial z} + \frac{g}{\Theta} \overline{w\theta} = K_m \left[\left(\frac{\partial U}{\partial z} \right)^2 + \left(\frac{\partial V}{\partial z} \right)^2 \right] - \frac{g}{\Theta} K_h \frac{\partial \Theta}{\partial z}. \quad (27)$$

The turbulent dissipation rate, ε , is related to E making use of a dissipation length l_ε ,

$$\varepsilon = \frac{(\alpha E)^{3/2}}{l_\varepsilon}. \quad (28)$$

If the dissipation length is assumed equal to the mixing length, then Eq. 20 reduces to,

$$K_m = \alpha^2 \frac{E^2}{\varepsilon}. \quad (29)$$

Delage's expression (18), using Dyer's stability functions (8), is used to describe the mixing-length profile $l_m = l_\varepsilon$.

As a one-dimensional unsteady model, it is necessary to prescribe the boundary conditions at the bottom and top of our discretized column domain. In addition, initial profiles are required to initialize the model. Surface-layer MOST is used to relate wall boundary conditions with the values of the near-wall cell (Alinot and Masson 2005). At the top boundary the velocity is taken equal to the geostrophic velocity and the fluxes of heat and momentum are set to zero.

Following Taylor and Delage (1971), a log-linear transform on the z axis is introduced in order to better accommodate the gradients in the bottom and the top of the boundary layer

$$Z_i = \ln \frac{z_i + z_0}{z_0} + \frac{z_i}{b_0}, \quad (30)$$

where b_0 is a constant that defines the extension of the linear contribution. A value of 67.5 m for b_0 is used as in Weng and Taylor (2003). Note that the coordinate transformation of Eq. 30 includes the roughness length z_0 as an offset to the z axis. This offset is also introduced in the surface-layer logarithmic law so that the roughness length values can be considered at the first grid point situated at $z = 0$.

The fluid equations are discretized with finite differences using backward Euler-implicit first-order time integration. Implicit time integration allows longer timesteps and better stability and convergence characteristics than explicit or semi-implicit methods. Diffusion terms are discretized with central differences using half-cell values for the eddy viscosity, i.e. a staggered grid.

5 Model Verification: The GABLS I Test Case

The GEWEX Atmospheric Boundary-Layer Study (GABLS) was conducted in 2001 to improve the understanding and the representation of the ABL in regional and large-scale climate models (Holtslag 2006). The methodology in GABLS I was to select a simple test case as a benchmark for comparison of state-of-the-art one-dimensional column models (Cuxart et al. 2006) and LES models (Beare et al. 2006).

The test case is based on the simulations presented by Kosovic and Curry (2000), where the boundary layer is driven by a prescribed uniform geostrophic wind with a specified cooling rate over a homogeneous ice surface. The simulation is run for 9 h until quasi-steady state is reached. The comparison of LES models (Beare et al. 2006) shows consistent results among the different models at different grid resolutions. Hence, they are a suitable reference for simpler one-dimensional models. In contrast, the intercomparison among one-dimensional

first-order closure models shows much larger scatter in the results (Cuxart et al. 2006). In general, it was found that the parametrizations used by numerical weather prediction models tend to overestimate the turbulent mixing, the surface friction and the boundary-layer depth.

The test case is defined by the following initial and boundary conditions: $f_c = 1.39 \times 10^{-4} \text{ s}^{-1}$; $U_g = 8 \text{ m s}^{-1}$; $V_g = 0$; $\Theta_0 = 265 \text{ K}$ for the first 100 m and then increasing at 0.01 K m^{-1} ; $E = 0.4(1 - z/250)^3 \text{ m}^2 \text{ s}^{-2}$ for the first 250 m and a minimum value of $10^{-9} \text{ m}^2 \text{ s}^{-2}$ above; $\overline{u\overline{w}} = 0.3E$; $\overline{v\overline{w}} = \overline{w\overline{\theta}} = 0$. The surface temperature Θ_0 starts at 265 K and decreases at a cooling rate of 0.25 K h^{-1} . The roughness length for momentum and heat is set to 0.1 m.

The GABLS I test case is run with the E - I_m model based on Dyer's stability functions. Both surface-layer and local scaling approaches are considered in order to better show the impact of local scaling. In addition, the results are compared with

- The Weng and Taylor (2006) (WT06 hereafter) E - I_m model, using a slightly different parametrization for the mixing and dissipation length scales. WT06 is the main reference for our modelling, which builds on the evaluation methodologies established for the GABLS I test case. Hence some of the model evaluation aspects used herein are common to WT06 for the sake of consistency.
- LES model runs using a 2-m resolution grid, from the LES model inter-comparison reported in Beare et al. (2006) (Beare06 hereafter). The data are available online at www.gabls.org.

All the simulations are made on a computational 1D domain of 1 km, using 301 cells and a timestep of 10 s. The configuration is similar to WT06, although WT06 uses a 4-km high column. A grid sensitivity, not shown, proves that almost the same results can be obtained with 50 vertical levels (Sanz Rodrigo 2011).

Figure 7 shows the evolution of the surface friction velocity, heat flux and Obukhov length and the boundary-layer height over the 9-h simulations. The boundary-layer height h_α is defined as the height where the shear stress falls to 5% of the surface value. Due to the continuous heat loss through the ground, the boundary layer as a whole cools down until a quasi-steady state is reached where the turbulent quantities are virtually time-independent. This occurs sooner for the friction velocity (after 5 h) than for the heat flux (after 7 h). The boundary-layer depth and the Obukhov length stabilize much earlier, after 1 and 2 h respectively.

The model based on local scaling is able to follow the evolution of the reference simulations whilst surface-layer scaling, although accurately reproducing the surface fluxes, overestimates the boundary-layer depth due to excessive turbulent mixing in the upper part of the boundary layer.

Figure 8 shows the vertical profiles of the velocity magnitude, the potential temperature, the shear stress and the heat flux at the end of the GABLS I simulation. The velocity profile shows a characteristic low-level jet that overshoots the geostrophic wind by 20%. Surface-layer scaling is seen to predict a deeper boundary layer due to overestimated shear stress and heat fluxes in the upper part of the boundary layer.

Sorbjan (2012) made a sensitivity analysis of a single-column model of the SBL using the GABLS I test case. He shows that when the cooling rate increases or the roughness length decreases the boundary layer becomes shallower, Ri increases and the turbulence level decreases; furthermore, the smaller the Coriolis parameter, the slower the evolution of the boundary layer. He also shows the important impact that subsidence can have in the upper part of the boundary layer.

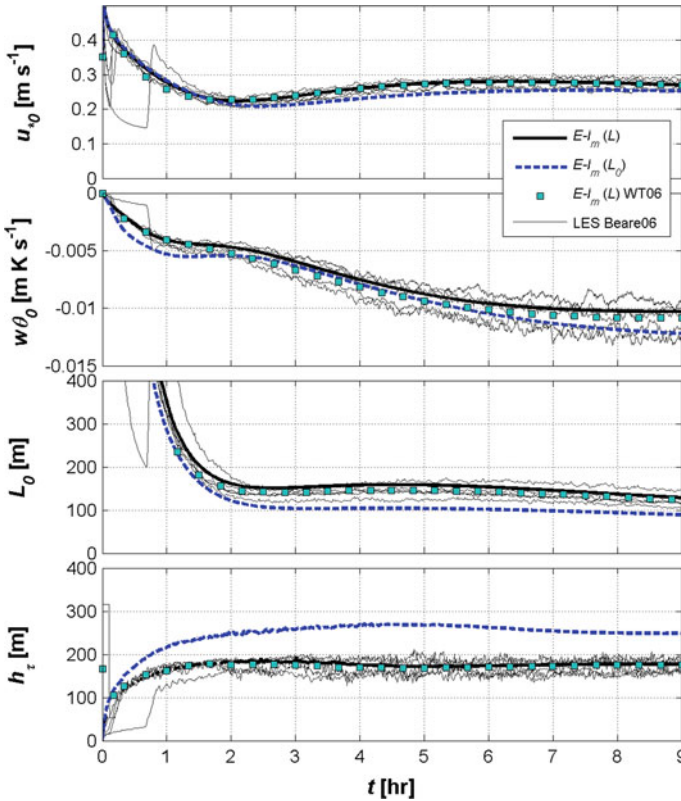


Fig. 7 Time evolution of surface friction velocity (u_{*0}), heat flux ($w\theta_0$), Obukhov length (L_0) and boundary-layer depth (h_i) of $E-l_m$ simulations based on local (L) and surface layer (L_0) scaling and compared with the $E-l_m$ model of WT06 and LES simulations of Beare06

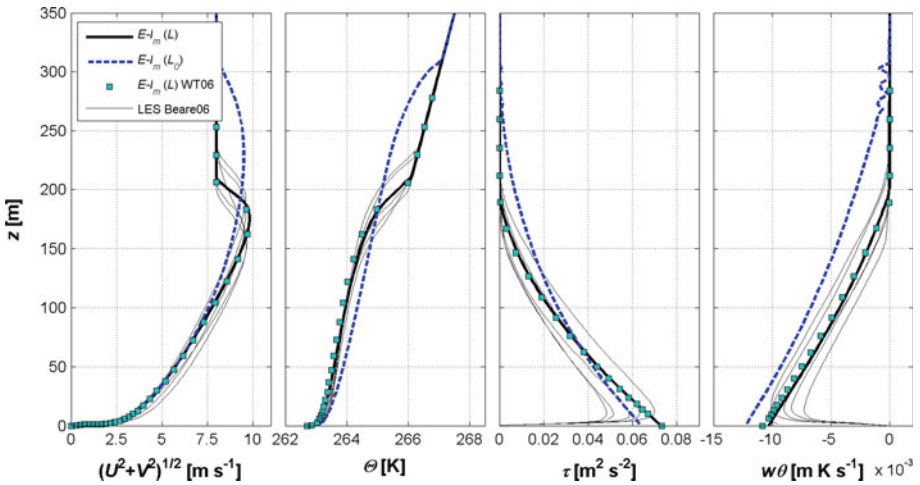


Fig. 8 Vertical profiles of mean wind speed, potential temperature (Θ), shear stress (τ) and kinematic heat flux ($w\Theta$) of $E-l_m$ simulations based on local and surface-layer scaling and compared with the $E-l_m$ model of WT06 and LES simulations of Beare06

6 Model Validation: The GABLS-Halley Mean Profiles

The GABLS I experiment was adapted to Halley conditions ($z_0 = 10^{-4}$ m, $f_c = -1.39 \times 10^{-4}$ s $^{-1}$) and run at different cooling rates, in the range from 0.125 to 2.5 K h $^{-1}$ as in WT06, in order to produce a family of 9-h long quasi-steady profiles (Table 2). The lapse rate of the inversion layer in the free atmosphere, 0.01 K m $^{-1}$, is left unaltered since it does not affect the shape of the final quasi-steady profiles (WT06).

Figures 1 and 2 show the simulations for 0.2 and 2.5 K h $^{-1}$ cooling in terms of the dimensionless velocity and temperature gradients. The profiles follow Dyer’s function (8), since it is the one adopted by the mixing-length parametrization. The curvature in the dimensionless velocity shear at $\zeta > 10$ denotes the presence of the low-level jet at the top of the boundary layer. This agrees well with Zilitinkevich et al. (2010), who argue that $\zeta \approx 10$ is the regime at which the boundary layer meets the free atmosphere, rather than attributing this effect to z -less stratification. The simulations show that the ζ value that makes the transition to the free atmosphere is higher at higher stabilities.

The transition to the free atmosphere is clearly noticed when plotting the flux Richardson number (Fig. 3). The runs follow Dyer’s formulation up to $\zeta \approx 1$ for the low cooling rate case and up to $\zeta \approx 4$ for the high cooling rate case. Above these values Ri_f increases above the critical flux Richardson number, $Ri_{fc} = 0.25$, by several orders of magnitude. The points above 0.25 are in the low-level jet region or above the boundary layer.

The family of profiles summarized in Table 2 is used to classify the boundary-layer stable regime in terms of a limited number of conditions. To validate this classification, the simulated quasi-steady profiles are compared with ensemble-averaged profiles under the same range of stability and friction velocity.

The surface boundary-layer parameters are referred to the 4-m level (subscript 4 in Table 1 and Figs. 9 and 10) as this is the lowest level with flux measurements. In order to account for the inertial characteristics of the cooled ABL, the interval between 4 and 9 h is considered. The surface friction velocity is limited to below 0.2 m s $^{-1}$ to ensure the absence of snowdrift in the measurements (Mann et al. 2000).

Figure 9 shows the simulated profiles at 0.25, 1 and 2.5 K h $^{-1}$ cooling rates. The resulting profiles have mean Obukhov lengths of 84.5, 19.4 and 6.6 m respectively at 4-m height ($\zeta_4 = 0.05, 0.21, 0.60$). The limiting values of L_4 at 4 and 9 h for each run are considered as the lower and upper limits of L_4 in the selection of the Halley profiles for ensemble averaging. In addition, a $\pm 10\%$ variation of the friction velocity around the simulated values at the 4-m level is allowed in the experimental data in order to select measured profiles with similar

Table 2 GABLS-Halley runs results after 4 and 9 h and considering the average profiles between 4 and 9 h

#	Cooling (K h $^{-1}$)	u_{*4} (m s $^{-1}$)			L_4 (m)			4/L Mean	16/L Mean	32/L Mean	h_t (m) Mean
		4 h	9 h	Mean	4 h	9 h	Mean				
1	0.125	0.17	0.19	0.19	183.6	141.3	164.9	0.02	0.11	0.25	157.7
2	0.25	0.16	0.18	0.18	93.1	71.9	84.5	0.05	0.21	0.51	146.8
3	0.5	0.15	0.16	0.16	44.6	34.9	41.2	0.10	0.45	1.16	130.1
4	1	0.13	0.14	0.14	20.7	16.3	19.4	0.21	1.04	3.12	108.9
5	1.5	0.12	0.12	0.13	13.1	10.1	12.2	0.33	1.78	6.37	77.0
6	2	0.11	0.11	0.12	9.5	7.1	8.7	0.46	2.70	11.85	44.4
7	2.5	0.11	0.10	0.11	7.3	5.3	6.6	0.60	3.82	21.37	38.7

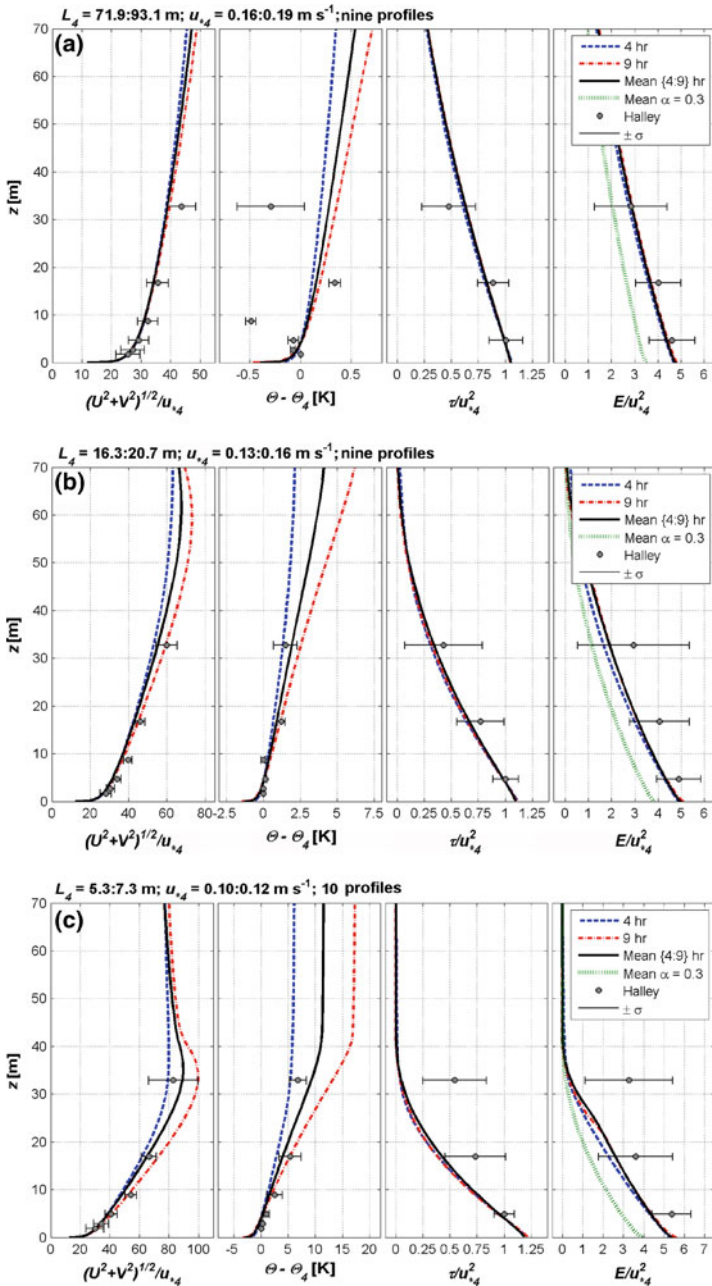


Fig. 9 Comparison of ensemble-averaged profiles at Halley and $E-l_m$ model simulations for a SBL with cooling rates of: **a** 0.25 K h^{-1} ; **b** 1 K h^{-1} ; **c** 2.5 K h^{-1} . The titles above each figure indicate the Obukhov length and friction velocity bins at 4-m level to filter each ensemble as well as the number of experimental profiles included. Ensemble-averaged profiles are provided with error bars indicating one standard deviation. The bins are consistent with Table 2 considering the variability of the simulations between 4 and 9 h. “Mean {4:9} h” indicate the simulated mean profile between 4 and 9 h using the Eq. 22 E parametrization and “Mean $\alpha = 0.3$ ” the mean profile using the default E parametrization based on constant α . Note the different limits in the X axes

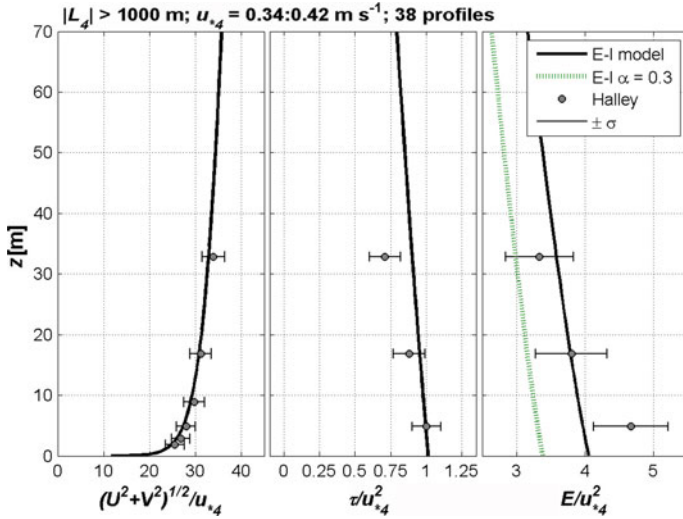


Fig. 10 Comparison of ensemble-averaged profiles at Halley and $E-l_m$ model simulations for neutral ABL conditions using (22) (“ $E-l$ model”) and using the default E parametrization based $\alpha = 0.3$ (“ $E-l \alpha = 0.3$ ”)

velocity. As a result around 10 hourly samples are extracted from the dataset for each class from which the mean and standard deviation (represented by error bars) are obtained.

The variability in the experimental profiles is quite high, attributed to the lack of homogeneity and stationarity of the profiles which is more apparent as the stability increases (Cullen et al. 2007). At low stabilities (Fig. 9a) temperature measurements are uncertain because the inversion is weak and the temperature difference between the levels is smaller than the measurement error of the sensors. Nevertheless, the mean profiles of velocity, potential temperature, shear stress and E are in fair agreement with the simulations. The E equation has been calibrated using the default constant value of $\alpha = 0.3$ and a stability dependent α according to (22). As expected, the site-specific calibration improves the prediction of E .

In the very stable case, the 32-m level seems to be placed within the low-level jet region. In this range ($\zeta = 21.4$) internal gravity waves are frequent and could enhance the momentum transfer, producing higher levels of E , as seen in Fig. 9; wave transfer cannot be resolved in a single-column model. The turbulence growth in the upper part of the boundary layer was described by Mahrt (1999) as an “upside-down” structure generated by vertical shear on the underside of the low-level jet. Sorbjan (2012) also showed that this structure cannot be simulated by a single-column model since it does not include the effects of internal gravity waves.

Handorf et al. (1999) found that the boundary-layer height at Neumayer Station (a similar site to Halley) under moderately to strongly stable stratification conditions is <45 m. Based on the simulated values of h_τ for Halley presented in Table 2 this is true for surface-layer stabilities, $\zeta > 0.4$.

Near-neutral steady-state conditions are simulated for a geostrophic wind speed of 16 m s^{-1} in order to increase the number of samples. The maximum mixing length is 31.1 m as predicted by Blackadar’s parametrization. The resulting boundary-layer depth is 709 m and the surface friction velocity is 0.34 m s^{-1} , higher than the threshold friction velocity for snowdrift. Hence blowing snow is present in these conditions (Mann et al. 2000).

Neutral profiles are extracted from the Halley dataset when $L_4 > 1,000$ m ($\zeta_4 < 4 \times 10^{-3}$). Again a $\pm 10\%$ interval around the 4-m friction velocity of the simulation is allowed to select experimental profiles with similar wind speeds. As a result, 38 profiles are retained.

The ensemble-averaged velocity profile is very accurately predicted by the steady-state neutral simulation. The first 70 m shown in Fig. 10 represent the first 10% of the ABL depth, i.e. the surface layer. In this region, the velocity profile is well described with the classical MOST wind law and, in this case, it fits the E - I_m model when using a roughness length of 0.7×10^{-4} m, in agreement with values $z_0 \sim 0.5 \times 10^{-4}$ m found by different authors at Halley (King and Anderson 1994).

In contradiction to surface-layer theory, the shear stress is not constant with height and shows a decay of 10% in the E - I_m simulation and 30% in the experimental data at 32 m. The value of E also shows a more rapid decay in the experimental data than in the simulation. While blowing snow causes rapid saturation of the boundary layer (Mann et al. 2000) and thence would not generate cooling, we speculate that buoyancy from suspended particles causes this suppression of turbulence. Again, the turbulence intensity can be calibrated with α based on the flux-profile measurements leading to better results than using the default value of 0.3.

The results confirm that quasi-steady profiles derived in stable and near-neutral conditions can be used as characteristic of ensemble-averaged wind conditions.

7 Conclusions

Flux-profile analysis of the Antarctic SBL at Halley using data from the 2003 experiment has been presented. In general, the same functional relationships found in mid-latitude sites apply at Halley, giving support to the universality of classical local scaling theories in the description of the horizontally homogeneous SBL.

Turbulence scaling is well characterized by mixing-length theory. The mixing-length parametrization of Delage (1974), based on the local Obukhov length, is suitable for first-order turbulence closure models. The dimensionless E/u_*^2 is found to be linearly dependent on the stability parameter ζ in the range 0.5–10. A simple functional relationship between turbulent kinetic energy and stability has been established.

Quasi-steady simulations of the SBL following the GABLS I approach have been validated against non-dimensional ensemble-averaged profiles for various stability classes. The performance of the mixing-length model is reasonably good in moderate stabilities. In the high stability range, the quasi-steady model cannot capture the increase of momentum and E observed in the upper part of the SBL, which could be due to the presence of gravity waves or advection that are not simulated by 1D models.

References

- Alinot C, Masson C (2005) k - ε Model for the atmospheric boundary layer under various thermal stratifications. *Trans ASME* 127:438–443
- Anderson PS (2009) Measurement of Prandtl number as a function of Richardson number avoiding self-correlation. *Boundary-Layer Meteorol* 131:345–362
- Baas P, Steeneveld GJ, van de Wiel H, Holtslag AAM (2006) Exploring self-correlation in flux-gradient relationships for stably stratified conditions. *J Atmos Sci* 63:3045–3054
- Beare RJ et al (2006) An intercomparison of large-eddy simulations of the stable boundary layer. *Boundary-Layer Meteorol* 118:247–272

- Blackadar AK (1962) The vertical distribution of wind and turbulent exchanges in neutral conditions. *J Geophys Res* 67:3095–3102
- Cheng Y, Brutsaert W (2005) Flux–profile relationships for wind speed and temperature in the stable atmospheric boundary layer. *Boundary-Layer Meteorol* 114:519–538
- Cullen NJ, Steffen K, Blanken PD (2007) Nonstationarity of turbulent heat fluxes at Summit, Greenland. *Boundary-Layer Meteorol* 122:439–455
- Cuxart J et al (2006) Single-column model intercomparison for a stably stratified atmospheric boundary layer. *Boundary-Layer Meteorol* 118:273–303
- Dabberdt WF (1970) A selective climatology of plateau station, Antarctica. *J Appl Meteorol* 9:311–315
- Delage Y (1974) A numerical study of the nocturnal atmospheric boundary layer. *Q J R Meteorol Soc* 100:251–265
- Djolv GD (1973) Modeling of the interdependent diurnal variation of meteorological elements in the boundary layer. Ph.D. thesis, University of Waterloo, Waterloo, ON, Canada
- Duykerke PG (1999) Turbulence, radiation and fog in Dutch stable boundary layers. *Boundary-Layer Meteorol* 90:447–477
- Dyer AJ (1974) A review of flux profile relationships. *Boundary-Layer Meteorol* 7:363–372
- Freedman FR, Jacobson MZ (2003) Modification of the standard k-equation for the stable ABL through enforced consistency with Monin–Obukhov similarity theory. *Boundary-Layer Meteorol* 106:383–410
- Garratt JR (1992) *The atmospheric boundary layer*. Cambridge University Press, UK, 316 pp
- Grachev AA, Fairall CW, Persson POG, Andreas EL, Guest PS (2005) Stable boundary-layer scaling regimes: the SHEBA data. *Boundary-Layer Meteorol* 116:201–235
- Grachev AA, Andreas EL, Fairall CW, Guest PS, Persson POG (2007a) SHEBA flux–profile relationships in the stable atmospheric boundary layer. *Boundary-Layer Meteorol* 124:315–333
- Grachev AA, Andreas EL, Fairall CW, Guest PS, Persson POG (2007b) On the turbulent Prandtl number in the stable atmospheric boundary layer. *Boundary-Layer Meteorol* 125:329–341
- Grachev AA, Andreas EL, Fairall CW, Guest PS, Persson POG (2012) Outlier problem in evaluating similarity functions in the stable atmospheric boundary layer. *Boundary-Layer Meteorol* 144:137–155
- Grachev AA, Andreas EL, Fairall CW, Guest PS, Persson POG (2013) The critical Richardson number and limits of applicability of local similarity theory in the stable boundary layer. *Boundary-Layer Meteorol* 147:51–82. doi:10.1007/s10546-012-9771-0
- Gryning S-E, Batchvarova E, Brümmner B, Jørgensen H, Larsen S (2007) On the extension of the wind profile over homogeneous terrain beyond the surface layer. *Boundary-Layer Meteorol* 124:251–268
- Handorf D, Foken T, Kottmeier C (1999) The stable atmospheric boundary layer over an Antarctic ice sheet. *Boundary-Layer Meteorol* 91:165–186
- Hogstrom U (1988) Non-dimensional wind and temperature profiles in the atmospheric surface layer: a re-evaluation. *Boundary-Layer Meteorol* 42:55–78
- Holt T, Raman S (1988) A review of comparative evaluation of multilevel boundary layer parametrizations for first-order and turbulent kinetic energy closure schemes. *Rev Geophys* 26:761–780
- Holtslag B (2006) Preface: GEWEX atmospheric boundary-layer study (GABLS) on stable boundary layers. *Boundary-Layer Meteorol* 118:243–246
- King JC (1990) Some measurements of turbulence over an Antarctic ice shelf. *Q J R Meteorol Soc* 116:379–400
- King JC, Anderson PS (1988) Installation and performance of the STABLE instrumentation at Halley. *Br Antarct Surv Bull* 79:65–77
- King JC, Anderson PS (1994) Heat and water vapour fluxes and scalar roughness lengths over an Antarctic ice shelf. *Boundary-Layer Meteorol* 69:101–121
- King JC, Turner J (1997) *Antarctic meteorology and climatology*. Cambridge University Press, UK, 409 pp
- Klipp CL, Mahrt L (2004) Flux–gradient relationship, self-correlation and intermittency in the stable boundary layer. *Q J R Meteorol Soc* 130:2087–2103
- König G (1985) Roughness length of an Antarctic ice shelf. *Polarforschung, Bremerhaven, Alfred Wegener Institute for Polar and Marine Research & German Society of Polar Research* 55:27–32
- Kosovic B, Curry JA (2000) A large eddy simulation study of a quasi-steady, stably stratified atmospheric boundary layer. *J Atmos Sci* 57:1052–1068
- Kouznetsov RD, Zilitinkevich SS (2010) On the velocity gradient in stable stratified sheared flows. Part 2: Observations and models. *Boundary-Layer Meteorol* 135:513–517
- Lettau HH, Dabberdt WF (1970) Variangular wind spirals. *Boundary-Layer Meteorol* 1:64–79
- Mahrt L (1999) Stratified atmospheric boundary layers. *Boundary-Layer Meteorol* 90:375–396
- Mahrt L, Vickers D (2003) Formulation of turbulent fluxes in the stable boundary layer. *J Atmos Sci* 60:2538–2548
- Mann GW, Anderson PS, Mobbs SD (2000) Profile measurements of blowing snow at Halley, Antarctica. *J Geophys Res* 105:24491–24508

- Nieuwstadt FTM (1984) The turbulent structure of the stable, nocturnal boundary layer. *J Atmos Sci* 41:2202–2216
- Sanz Rodrigo J (2011) On Antarctic wind engineering. Ph.D. thesis, Univeristé Libre de Bruxelles and von Karman Institute for Fluid Dynamics, Belgium
- Sorbjan Z (1986) On similarity in the atmospheric boundary layer. *Boundary-Layer Meteorol* 34:377–397
- Sorbjan Z (1989) Structure of the atmospheric boundary layer. Prentice-Hall, Englewood Cliffs, 317 pp
- Sorbjan Z (2010) Gradient-based scales and similarity laws in the stable boundary layer. *Q J R Meteorol Soc* 136:1243–1254
- Sorbjan Z (2012) A study of the stable boundary layer based on a single-column K-theory model. *Boundary-Layer Meteorol* 142:33–53
- Sorbjan Z, Grachev AA (2010) An evaluation of the flux–gradient relationship in the stable boundary layer. *Boundary-Layer Meteorol* 135:385–405
- Sun J (2011) Vertical variations of mixing length under neutral and stable conditions during CASES99. *J Appl Meteorol Clim* 50:2030–2041
- Taylor PA, Delage Y (1971) A note on finite-difference schemes for the surface and planetary boundary layers. *Boundary-Layer Meteorol* 2:108–121
- Vickers D, Mahrt L (2003) The cospectral gap and turbulent flux calculations. *J Atmos Ocean Technol* 20:660–672
- Weng W, Taylor PA (2003) On modelling the one-dimensional atmospheric boundary layer. *Boundary-Layer Meteorol* 107:371–400
- Weng W, Taylor PA (2006) Modelling the one-dimensional stable boundary layer with an E-1 turbulence closure scheme. *Boundary-Layer Meteorol* 118:305–323
- Wyngaard JC, Coté OR (1972) Cospectral similarity in the atmospheric surface layer. *Q J R Meteorol Soc* 98:590–603
- Yagüe C, Redondo JM (1995) A case study of turbulent parameters during the Antarctic winter. *Antarct Sci* 7:421–433
- Yagüe C, Maqueda G, Rees JM (2001) Characteristics of turbulence in the lower atmosphere at Halley IV station, Antarctica. *Dyn Atmos Ocean* 34:205–223
- Zilitinkevich S, Baklanov A (2002) Calculation of the height of the stable boundary layer in practical applications. *Boundary-Layer Meteorol* 105:389–409
- Zilitinkevich SS, Esau IN (2007) Similarity theory and calculation of turbulent fluxes at the surface for the stably stratified atmospheric boundary layer. *Boundary-layer Meteorol* 125:193–205
- Zilitinkevich SS, Mammarella I, Baklanov AA, Joffre SM (2008) The effect of stratification on the aerodynamic roughness length and displacement height. *Boundary-Layer Meteorol* 129:179–190
- Zilitinkevich SS, Esau I, Kleeorin N, Rogachevskii I, Kouznetsov RD (2010) On the velocity gradient in stably stratified sheared flows. Part 1: Asymptotic analysis and applications. *Boundary-Layer Meteorol* 135:505–511
- Zilitinkevich SS, Elperin T, Kleeorin N, Rogachevskii I, Esau I (2013) A hierarchy of energy- and flux-budget (EFB) turbulence closure models for stably-stratified geophysical flows. *Boundary-Layer Meteorol* 146:341–373. doi:10.1007/s10546-012-9768-8